Journal of Cleaner Production 237 (2019) 117855

Contents lists available at ScienceDirect

Journal of Cleaner Production

journal homepage: www.elsevier.com/locate/jclepro

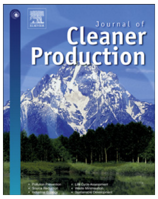

Spectroscopic analyses combined with Gaussian and Coats-Redfern models to investigate the characteristics and pyrolysis kinetics of sugarcane residue-derived biochars

Fanhao Song [a, b, 1], Xiaojie Wang [c, 1], Tingting Li [a], Jin Zhang [a], Yingchen Bai [a, *], Baoshan Xing [d], John P. Giesy [a, e], Fengchang Wu [a]

[a] *State Key Laboratory of Environmental Criteria and Risk Assessment, Chinese Research Academy of Environmental Sciences, Beijing, 10012, China*
[b] *College of Water Sciences, Beijing Normal University, Beijing, 100875, China*
[c] *Guangdong Provincial Key Laboratory of Environmental Pollution Control and Remediation Technology, School of Environmental Science and Engineering, Sun Yat-Sen University, Guangzhou, 510006, China*
[d] *Stockbridge School of Agriculture, University of Massachusetts, Amherst, MA, 01003, USA*
[e] *Department of Biomedical and Veterinary Biosciences and Toxicology Centre, University of Saskatchewan, Saskatoon, Saskatchewan, SK, S7N 5B3, Canada*

ARTICLE INFO

Article history:
Received 8 January 2019
Received in revised form
23 June 2019
Accepted 31 July 2019
Available online 1 August 2019

Handling editor:Prof. S Alwi

Keywords:
Biomass
Functional groups
Carbon condensation
Aromatic cluster size
Thermal degradation

ABSTRACT

Biomass and biochars are considered good potential materials for environmental applications and their positive or negative effects on an ecosystem are mainly derived from the diverse physicochemical and pyrolytic kinetic properties. However, the characteristics of biomass resulted biochars have not been fully recognized. In this study, three biochars derived from dried sugarcane residue were prepared under 300, 500 and 700 °C. Spectroscopic techniques coupled with a Gaussian model were applied to innovatively de-convolute the existences and contributions of distinct overlapping peaks in the spectra, and then quantitatively evaluated the functional groups, sizes of aromatic clusters, and the degree of aromatic condensation of the sugarcane residue and biochars. Aromatic carbon/carbon-carbon double bond, single bonded oxygen, and pyrrolic nitrogen were dominant surface elements of the sugarcane residue and biochars. Decomposition and formation of different functional groups were quantitatively distinguished for pyrolysis temperature dependent biochars by Gaussian model. The changes of different carbon types and structures were attributed to the progressive dehydration, decarboxylation, aromatization reactions and structural formations of condensed carbon during the conversion of sugarcane residue into biochars. The biochars produced at higher pyrolysis temperatures exhibited higher fractions of bridgehead carbons, aromatic ring cluster sizes, and macromolecular aromatics. The sugarcane residue and biochars had fewer substituent groups at each aromatic ring and the biochars produced under 500 °C and 700 °C had an average of 14 more carbons in average aromatic cluster. The pyrolysis reactions of sugarcane residue and biochars were mainly associated with the degradation of hemicellulose, cellulose, and lignin components. The novel application of using spectroscopy coupled with a Gaussian model presented in this study has shown great potential as a valuable and effective characterization technique for studying the characteristics and pyrolysis kinetics of biochars. Results from this study benefit the greater understanding of the properties and reactivity of biomass and biochars, and their effects on pyrolysis optimization, carbon/pollutant sequestration, potential energy generation, and many other applications in the future.

1. Introduction

As one renewable and sustainable energy source, the development and utilization of biomass and other waste materials (e.g., biosolids or organic fraction of solid waste) have attracted significant attentions (Galil and Yaacov, 2011; Giudicianni et al., 2015).

---

* Corresponding author.
E-mail address: baiyc@craes.org.cn (Y. Bai).

[1] Fanhao Song and Xiaojie Wang contributed equally to this work.

https://doi.org/10.1016/j.jclepro.2019.117855

The effective use of biomass or other materials has the potential to reduce the greenhouse gases emissions and to recycle the biochars (BCs) and liquid-state energy products, improving the energy consumption and environmental protection (Chen et al., 2009). For example, the biomass from agriculture and livestock activities contributes significantly to anthropogenic ammonia and carbon dioxide emissions to air; therefore, the rational control of pyrolysis process of biomass is beneficial to reduce the eutrophication of water courses/ecosystems and the acidification of water/soil caused by greenhouse gases (Balsari et al., 2007; Scotto Di Perta et al., 2016). Additionally, the valuable products of BCs refer to heterogeneous and carbonaceous materials formed during oxygen-limited pyrolysis of a variety of biomass materials (Bachmann et al., 2016). The heterogeneous properties of BCs are associated to the individual BCs particles and the originating feedstocks or different pyrolysis conditions (Verheijen et al., 2010). BCs are a recalcitrant form of carbon and can be useful in the remediation of soils by sequestration of organic molecules (Ahmad et al., 2014; Singh and Cowie, 2014). As a soil amendment for agricultural applications, BCs offer benefits such as improving physical properties and the fertility of soils, increasing soil cation exchange, and nutrient retention capacity like organic matters, all of which can improve crop yields (Song et al., 2019; Wang et al., 2019). However, the combined the heterogeneity and the wide range of physicochemical properties and chemical reactions, the effects of BCs on a variety of soil properties are somewhat unpredictable, which bring the difficulties to make a general assessment of potential risks once deployed BCs into soils (Calvelo Pereira et al., 2011; Joeri et al., 2017). Therefore, the detailed characterization of BCs is important and its application to soil should be considered not only for heterogeneous structures or functions among BCs, but also for various soil types and environmental conditions (Verheijen et al., 2010). Biochemically, a variety of structures and functional groups can be involved in modulating the mobility and reactivity of BCs, as well as sorption of contaminants such as metal ions ($Cu^{2+}$and Zn^{2+}) or organic compounds (e.g., polycyclic aromatic hydrocarbons) (Alam et al., 2018; Shen et al., 2018). In particular, the aromatic cluster size, bridgehead aromatic carbons, and the number of aromatic rings can affect the fate and transport of contaminants in soil systems by regulating the adsorption capacities of BCs (Qu et al., 2016). Despite the significance, there is still lack of an understanding of the properties of aromatic structures of BCs that contribute to desirable environmental benefits such as soil carbon recalcitrance and sequestration.

The temperature of pyrolysis is one of the primary factors regulating the structures and functions of BCs derived from biomass (Tang et al., 2019). Investigating the structural and functional characteristics of BCs as a function of pyrolysis temperature (PT) is important for a better understanding of the long-term environmental significance of BCs produced at various temperatures of pyrolysis (Zhao et al., 2018). Many studies have investigated the inverse relationship between the polarity of BCs and the temperature of pyrolysis via elemental analysis, X-ray photon spectroscopy (XPS) and Fourier transform infrared (FTIR) spectroscopy (Norwood et al., 2013; Singh and Cowie, 2014). For example, the increased aromatic structures and decreased O-H and -CH_3 groups as a function of temperature have been confirmed by FTIR analysis (Qu et al., 2016). The esters, measured by FTIR, were almost completely eliminated due to carbonization by pyrolysis of esters in BCs at high temperatures (≥500 °C) (Chen et al., 2015). Non-protonated aromatic carbons in BCs, measured by solid-state ^{13}C nuclear magnetic resonance (NMR) spectroscopy, were reported to be proportional to temperature of pyrolysis (Cao et al., 2012). As would be expected in such a complex, multicomponent systems, the bands in XPS, FTIR, and ^{13}C NMR spectra related to specific components in BCs were shown to be generally rather broad and featureless or overlapping (Liu et al., 2014, 2018). The Gaussian model (GM) was a useful, quantitative method to distinguish these overlaps and reveal “hidden” peaks during spectroscopic analyses (Liu et al., 2016; Tian et al., 2016). This study aimed to quantitatively investigate the functional groups and structures of SCR-derived BCs using spectroscopic techniques combined with GM to better understand the potential effects of pyrolysis temperature on the BCs properties.

The biomass pyrolysis has been widely used as a potential renewable energy resource for power or energy generation (Waqas et al., 2018). Pyrolysis of the main components (e.g., hemicelluloses, cellulose, and lignin) in biomass or BCs was considered the superposition mechanism, which was the point of greatest interest for research. Additionally, the determination of kinetic parameters of biomass or BCs provided information on the thermal events occurring, as well as their structures and compositions (Gao et al., 2013). In the investigation of kinetics, the Coats-Redfern model has been used to compute the activation energy, providing a more effective visualization of the results and fitting of the thermogravimetric (TG) and derivative thermogravimetric (DTG) curves (Thakur et al., 2018). Recently, the pyrolysis kinetics of different biomass materials, such as palm kernel shell, has been studied by use of TG combined with a pyrolysis model (Ma et al., 2015). However, there is less available in the literature on the kinetic evaluation of SCR and SCR-derived BCs using a TG-Coats-Redfern method. Based on the characterization of SCR and SCR derived BCs using elemental analysis and spectroscopic techniques (e.g., XPS, FTIR, and ^{13}C NMR), therefore, the major objectives of this work were to 1) evaluate their variation of elemental compositions, functional groups, carbon distributions and skeleton structure types, such as clusters of aromatic groups, bridgehead aromatic carbon, and degrees of substitution of aromatic rings; 2) deconvolute the overlapping peaks in spectra and quantify their temperature-dependent functional groups and carbon types by novel XPS/FTIR/NMR—Gaussian method; 3) investigate the their pyrolysis behaviors and kinetics using TG analysis coupled with Coats-Redfern model.

2. Materials and methods

2.1. Preparation of SCR and BCs

Sugar cane (*Saccharum officinarum* L.) residue (SCR) was obtained from the Sugarcane Research Institute, Guangzhou Province, China. The SCR was dried at 100 °C for 3 h to reach a constant mass and ground into fine particles with relative small size by use of a pulverizer. The SCR with small particle size has relative greater heated area, which is beneficial to obtain the thoroughly pyrolyzed BCs with structural features that less affected by SCR configuration (Şensöz et al., 2000). Three BCs were prepared from SCR pyrolysis in a GDL-1,500X tubular furnace (Kejin, Hefei, China). In details, approximately 2.5 kg of SCR were placed into a main furnace chamber in batches, and the furnace was thoroughly purged with nitrogen to empty the oxygen inside the chamber. The pre-dried SCR was pyrolyzed in a heated chamber with the temperature of pyrolysis increasing from 25 °C to 250 °C for 40 min. The pyrolysis temperature of SCR increased from ambient to each target temperature (i.e., 300 °C, 500 °C, and 700 °C) with a heating rate of $10\,^{\circ}C\cdot min^{-1}$, and holding at each target temperature for 40 min. After completion of SCR pyrolysis, resulting BCs identified as BC300, BC500 and BC700 were cooled to room temperature under nitrogen purge, which was beneficial to reduce the rapid oxidation and auto-ignition of BCs. The BC300, BC500 and BC700 were sieved with 0.3 mm sieves and stored in a glass container before analyses. For the further analyses, the SCR and BCs were reground and passed through a 200-mesh sieve to achieve their particle size less than 75 μm.

2.2. Characterization of SCR and BCs

Elemental compositions of SCR and BCs were determined by use of an elemental analyzer (Elementar vario, macro EL, Germany) according to a previously published method (Qu et al., 2016). Ash contents of SCR and BCs were measured by combustion at 750 °C for 5 h. Electrical conductivity (EC) and pH values of the BCs were measured in a 1:20 (*w*:*v*) volume ratio with H_2O using a conductivity meter and a pH meter (Mettler Toledo, China), respectively. XPS measurements of SCR and BCs were performed on a PHI 5,000 Versaprobe (ULVAC-PHI, Japan) using a monochromatized AlKα radiation as the excitation source ($h\nu = 1{,}486.6$ eV). Before FTIR analysis, SCR and BCs were finely ground to powder together with KBr in an agate mortar. FTIR spectra of SCR and BCs were recorded by use of an FTIR spectrometer (Nicolet is5, Thermo Scientific, MA, USA) at wavenumbers from 700 to 4,000 cm^{-1} with a resolution of 4 cm^{-1}. Background spectra were obtained and then subtracted from FTIR spectra of SCR and BCs. Solid-state ^{13}C-NMR spectra of SCR and BCs were obtained with a Bruker Avance AV-400 (Bruker Corp., Billerica, MA, USA) spectrometer at 400 Hz, with a repetition time of 110.7 ms with echo time of 4.5 ms.

2.3. Deconvolution of XPS, FTIR and ^{13}C NMR spectra by use of Gaussian model

To obtain more details on the functional and structural characteristics of SCR and BCs, a Gaussian model (GM) was used to determine the presence of distinct bands that were overlapping or hiding in the original XPS, FTIR, and ^{13}C NMR spectra. XPS spectra were analyzed and de-convoluted using XPSPEAK software with 20% Gaussian-Lorentzian value. A Shirley background correction was used to remove background noise for XPS (Singh et al., 2014). For curve fittings of both FTIR and ^{13}C NMR spectra, the Loess algorithm and 2nd Derivative Zero algorithms were selected to smooth and subtract the baseline of the spectra, respectively. Fitting of FTIR and ^{13}C NMR spectra were accomplished by use of the second-derivative method, and "Peak types" used for fitting of functions to spectra were set as "Spectroscopy" and "Gauss Amp" in GM. Fitting peaks were optimized by modifying peak height, width, and shape until the correlation coefficient (R^2) value between the original spectra and fitted curves was close to 1.0, which corresponded to minimal variance.

2.4. Thermodynamic behaviors and kinetics of SCR and BCs

The TG analysis of SCR and BCs was conducted by a thermogravimetric analyzer (TGA Q5,000, TA Instruments, USA). Samples of 10 mg were placed into an alumina crucible and heated at a heating rate of 10 °C·min^{-1} from ambient temperature to 850 °C. High-purity nitrogen was used as a purge and protective gas at a flow rate of 60 mL min^{-1}. The Coats-Redfern model is considered to be one mathematical model based on the certain physico-geometrical assumptions with respect to the reactants shape and the reaction driving force (Sánchez-Jiménez et al., 2013). Two limitations may be considered for applications of the Coats-Redfern model to real systems. Firstly, the Coats-Redfern model may not be fulfilled in a real system or process due to it is built on the strict assumptions (Sánchez-Jiménez et al., 2013). Secondly, the Coats-Redfern model is possible inadequate to describe the non-isothermal study of reactions (e.g., dehydrations) with low activation energy or temperature ranges (< 200 °C) (Coats and Redfern, 1964; Sánchez-Jiménez et al., 2013). However, the Coats-Redfern model has been widely used for performing the kinetic modeling of the biomass pyrolysis due to its simplicity to deal with the primary degradation region of TG curve (Thakur et al., 2018). In addition, the Coats-Redfern method is convenient to calculate the kinetic parameters based on the pyrolysis data at just one heating rate (Krishna and Pugazhenthi, 2011). Determination of kinetic parameters was critical to understand and optimize the process of thermal decomposition of SCR and BCs. In this study, the Coats-Redfern model was used to calculate the thermodynamic behaviors and kinetics of SCR and BCs at different temperature ranges (>200 °C). The rate constant (*k*) of the pyrolysis reaction could be calculated following the Arrhenius Law (Coats and Redfern, 1964; Thakur et al., 2018).

$$k(T) = A\,exp\left(-\frac{E_\alpha}{RT}\right) \tag{1}$$

where A is the pre-exponential factor (s^{-1}), E_a is the activation energy ($KJ\cdot mol^{-1}$), R is universal gas constant ($R = 8.3145\ J\ mol^{-1}\cdot k^{-1}$), and T is the absolute temperature (K). In addition, the E_a represents the minimum energy requirement for a reaction to start, or in other words, a higher E_a indicates that thermal decomposition is more difficult.

The general decomposition rate of SCR and BCs could be expressed as:

$$\frac{d\alpha}{dt} = k(T)\cdot(1-\alpha) \tag{2}$$

where α is the conversion ratio of the decomposed sample, t is the decomposition time, and $f(\alpha)$ is a function representing the reaction mechanism. The conversion ratio α could be calculated from Eq. (3):

$$\alpha = \frac{m_0 - m_t}{m_0 - m_f} \tag{3}$$

where m_0 is the initial sample mass; m_t is the sample mass at time t; and m_f is the sample mass after complete decomposition.

Thus, by combining Eqs. (1) and (3), the degradation reaction Eq. (2) could be written as:

$$\frac{d\alpha}{dT} = \frac{A}{\beta}\,exp\left(-\frac{E_\alpha}{RT}\right)\cdot(1-\alpha) \tag{4}$$

where β is the constant heating rate, which can be expressed as $\beta = \frac{dT}{dt}$.

By re-arranging and integrating Eq. (4), an equation can be obtained as:

$$\int_0^\alpha \frac{d\alpha}{(1-\alpha)} = \frac{A}{\beta}\cdot\int_0^T exp\left(-\frac{E_\alpha}{RT}\right)\cdot dT \tag{5}$$

The final from of Coats-Redfern model can be obtained as Eq. (6):

$$ln\left\{\frac{-ln\,(1-\alpha)}{T^2}\right\} = ln\left\{\frac{AR}{\beta E_\alpha}\cdot\left(1-\frac{2RT}{E_\alpha}\right)\right\} - \frac{E_\alpha}{RT} \tag{6}$$

For most observed E_α value, $E_\alpha \gg RT$, hence $\frac{2RT}{E_\alpha} \approx 0$ and $\left(1-\frac{2RT}{E_\alpha}\right) \approx 1$, thus Eq. (6) can be written as:

$$ln\left\{\frac{-ln\,(1-\alpha)}{T^2}\right\} = ln\left(\frac{AR}{\beta E_\alpha}\right) - \frac{E_\alpha}{RT} \tag{7}$$

By plotting $1/T$ against $ln\left\{\frac{-ln\,(1-\alpha)}{T^2}\right\}$, a straight line with slope of $-\frac{E_\alpha}{RT}$ and intercept of $ln\left(\frac{AR}{\beta E_\alpha}\right)$ were obtained, so that E_α and A were determined.

3. Results and discussion

3.1. Physiochemical and surface properties of SCR and BCs

Elemental composition, atomic ratio, pH, and EC values of SCR and BCs are summarized in Table 1. Proportions of C of SCR and BCs, expressed on a mass basis from elemental analysis (EA), increased from 46.10% to greater than 66%, while H contents decreased from 6.01% to 1.39% as a function of increasing pyrolysis temperatures (IPT) (Table 1). Oxygen (O) contents of SCR and BCs from EA decreased from 44.6% to 8.29% with IPT (Table 1). Similar trends in elemental composition with IPT were also reported for BCs from various sources, such as wood and rice straw (Cao et al., 2012; Wu et al., 2012). In addition, both H/C and O/C ratios of SCR and BCs from EA progressively decreased as a function of IPT (Table 1), which was related to progressive dehydration and decarboxylation, as well as formation of structures containing condensed carbon during pyrolysis (Wu et al., 2012). In a Van Krevelen diagram, SCR, BC300, BC500, and BC700 were located in the biomass/cellulose zone, lignin/melanoidin zone, coal zone, and black carbon/soot zone, respectively (Fig. S1) (Jin et al., 2018). Therefore, the broad compositional fields in the Van Krevelen diagram were attributed to the great effects on the structural heterogeneity and different chemical compositions under different PTs (Jin et al., 2018). Moreover, the atomic ratio of (O + N)/C of SCR and BCs from EA decreased from 0.74 to 0.10 with IPT (Table 1), indicating that the BC produced at higher temperatures was less polar. The ash contents of BCs with range of 14.80%–23.60% were much higher than that of SCR (2.79%) (Table 1), indicating that the accumulation of mineral components during the SCR pyrolysis process. Bachmann et al. (2016) also reported that the degradation of organic matters during the pyrolysis resulted in a relative ash enrichment. Values of pH (range: 6.91–9.92) and EC (range: 1.73–5.34 mS cm^{-1}) of BCs were elevated with IPT (Table 1). The BCs produced at higher temperatures had lower polarity and higher EC values, which was probably more due to the enhanced concentration of inherent minerals in BCs caused by loss of volatiles (Kloss et al., 2012).

Contents of C on surfaces of SCR and BCs from XPS were in the range of 70.43%–91.06% (Table 1). Surface enrichment of C was calculated as the ratio between XPS-based C contents and those obtained from the EA, indicating the heterogeneous spatial distributions of elements. Values of surface enrichment of C of SCR and BCs ranged 1.27–1.59 (Table 1), which indicated that the C enriched at particle surfaces of SCR and BCs, especially for SCR and BC300. The surface O contents and (O + N)/C ratios of SCR and BCs from XPS were inversely proportional with IPT (Table 1), which was in agreement with the trends observed from the EA. Curve fittings for C1s, N1s, and O1s spectra from the original XPS were established, and the relative area (RA) of different species of elements on surfaces was determined (Fig. 1 and Table S1). For the XPS C1s spectra, the largest RA was corresponded to C=C/aromatic C (64.94%–93.68%), followed by phenolic C (6.32%–30.50%) and aliphatic/carboxylic C (4.55%) on SCR and BCs surfaces (Table S1). The RAs of phenolic C (30.50%) and aliphatic/carboxylic C (4.55%) were largest on SCR surfaces (Table S1). The RAs of C=C/aromatic C (78.35%–93.68%) on BCs surfaces were larger than those (64.94%) on SCR surfaces (Table S1). These results were consistent with the inverse relationship between O contents and PT. For the XPS O1s spectra, the O in hydroxyl groups with RA of 86.56% was dominant on SCR surfaces, while the ether-O in ester structures were richest on BC surfaces with RAs of 48.45%–75.67% (Table S1). Therefore, the single-bonded O is the main component on SCR and BC surfaces. The O in carbonyl groups on SCR and BC surfaces ranged from 13.44% to 51.55%, and generally showed increases with IPT (Table S1). For the XPS N1s spectra, pyrrolic N accounted for more than 61.31% were richest in all organic N structures on SCR and BCs surfaces (Table S1). Chemisorbed N with RAs of 16.82%–38.69% mainly appeared on BC500 and BC700 surfaces (Table S1), indicating that the N existed in hetero-aromatic N structures formed during pyrolysis (Singh et al., 2014). In the presented study, the heteroatoms (e.g., O and N) incorporated within the aromatic rings were presented for SCR and BCs, which are likely great contributions to their highly heterogeneous surface chemistry (Verheijen et al., 2010). Although the complexity and heterogeneity affect the chemical composition and surface chemistry of various types of biochar to a certain extent, it is hope that the results of physiochemical and surface properties of SCR and BCs will help further explain the way SCR-derived BCs interact with various organic and inorganic compounds in soil or water environments.

3.2. Evolution of specific functional groups in SCR and BCs

FTIR spectra were used to obtain information on functional groups of SCR and BCs. To investigate active functionalized H and unsaturated structures in SCR and BCs, the regions at 3,730–2,400 cm^{-1} and 1,800–1,450 cm^{-1} in FTIR spectra of samples were de-convoluted into 6–8 and 9–11 individual peaks, respectively, by using a GM ($R^2 = 0.964–0.999$) (Figs. 2 and S2). Origins, positions, and RAs of Gaussian fitting peaks from FTIR spectra were distinguished and calculated according to previously published results (Tables 2 and S2) (Liu et al., 2014; Tian et al., 2016). In the active functionalized H region (3,730–2,400 cm^{-1}), specific functional groups of SCR and BCs primarily included H-bonded carboxylic groups (2,556 cm^{-1}), -COOH groups (2,695–2,649 cm^{-1}), aromatic C-H stretching vibration (3,094–3,038 cm^{-1}), -OH···N groups (3,006–2,801 cm^{-1}), tightly bound cyclic -OH tetramers (3,180–3,143 cm^{-1}), and free OH

Table 1
Elemental composition, atomic ratio, pH and EC values of SCR and BCs.

Biochars	Bulk Elemental Composition									Surface Elemental Composition				Surface enrichment of C[b]	pH (H_2O)	EC (mS·cm^{-1})
	Mass percentages (%)				Ash (%)[a]	Atomic ratio				Mass percentages (%)			Atomic ratio			
	C	H	O	N		H/C	O/C	C/N	(O + N)/C	C	O	N	(O + N)/C			
SCR	46.10	6.01	44.6	0.50	2.79	1.57	0.73	107.55	0.74	70.43	25.89	2.64	0.41	1.53	nd[c]	nd
BC300	53.07	3.62	18.9	0.81	23.60	0.82	0.27	76.43	0.28	84.21	13.08	1.65	0.17	1.59	6.91	1.73
BC500	67.86	3.24	13.0	1.10	14.80	0.57	0.14	71.96	0.16	85.90	10.92	2.14	0.15	1.27	9.92	2.43
BC700	66.60	1.39	8.29	0.68	23.04	0.25	0.09	114.25	0.10	91.06	6.49	1.36	0.09	1.37	9.36	5.34

[a] Total O was derived by subtraction as follows: O (%) = 100-ash (%)-C (%)-H (%)-N (%).
[b] Surface enrichment of C = C (XPS)/C (EA).
[c] Not detected.

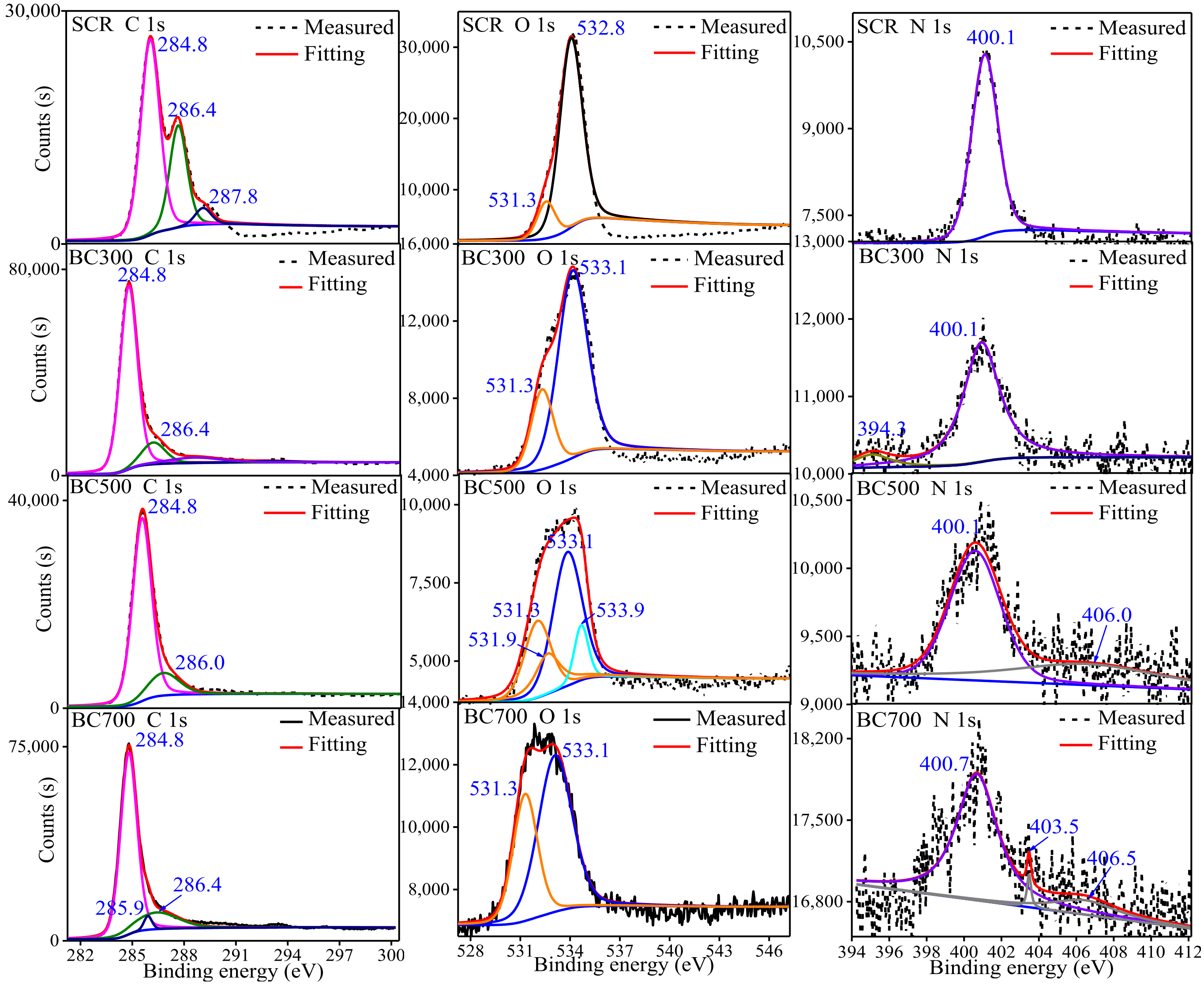

Fig. 1. Fitting curves of XPS C1s, O1s and N1s spectra of SCR and BCs.

Table 2
Assignments and relative area of Gaussian fitting peaks at 3,730–2,400 cm^{-1} region in the FTIR spectra of SCR and BCs.

SCR			BC300			BC500			BC700		
Wav. (cm^{-1})[a]	Assignment	RA (%)[b]	Wav. (cm^{-1})	Assignment	RA (%)	Wav. (cm^{-1})	Assignment	RA (%)	Wav. (cm^{-1})	Assignment	RA (%)
2,689	-COOH dimers	10.85	2,649	-COOH dimers	13.19	2,401	P-H phosphine groups	27.72	2,679	-COOH dimers	21.03
2,801	-OH···N (acid/base structures)	2.44	2,785	O-CH_3 or N-CH_3	5.00	2,556	H bonded carboxylic groups	30.95	2,836	-OH···N (acid/base structures)	12.51
2,998	-OH···N (acid/base structures)	4.33	3,006	-OH···N (acid/base structures)	4.39	2,695	-COOH dimers	15.32	2,972	-OH···N (acid/base structures)	2.05
3,094	aromatic CH stretching vibration	9.40	3,067	aromatic CH stretching vibration	8.78	2,807	-OH···N (acid/base structures)	12.09	3,038	aromatic CH stretching vibration	24.55
3,542	OH … π	6.13	3,170	tightly bound cyclic OH-tetramers	15.35	2,985	-OH···N (acid/base structures)	3.81	3,180	tightly bound cyclic OH-tetramers	16.63
3,727	free OH groups	66.84	3,556	OH … π	13.04	3,054	aromatic CH stretching vibration	5.82	3,300	OH … OR	3.58
			3,701	free OH groups	40.25	3,143	tightly bound cyclic OH-tetramers	4.29	3,548	OH … π	4.55
									3,700	free OH groups	15.09

[a] Wav. was wavenumbers.

[b] Relative area (RA) (%) of each peak was calculated as dividing peak area of each fitting peak by the sum of the peak area of all the fitting peaks.

groups (3,730–3,727 cm^{-1}) (Fig. S2 and Table 2). The RAs of -COOH dimers increased from 10.85% to 21.03% as a function of IPT (Table 2). Larger RAs of -OH•••N groups (14.56%–15.90%) for BC500 and BC700 were observed compared to those (4.39%–6.77%) for SCR and BC300 (Table 2). However, both SCR and BC300 showed larger RAs of free -OH groups (40.25%–66.84%) and -OH … π groups (3,556–3,542 cm^{-1}, 6.13%–13.04%) compared to both BC500 and BC700 (Table 2). The instabilities of both free -OH groups and -OH … π groups were consistent with previously reported results of the pyrolysis structures of brown coal (Xiong et al., 2015). The -OH … OR groups located at 3,300 cm^{-1} appeared in BC700 with an RA of 3.58% (Table 2). Considering the heterogeneity of SCR and BCs, the aliphatic hydrocarbons were unstable and likely decomposed to methane, carbon dioxide, and other gases, or formed as aromatic structures with IPT (Jin et al., 2016).

Various, specific functional groups in unsaturated structures (1,800–1,450 cm^{-1}) of SCR and BCs mainly included deformed vibration asymmetric -CH$_3$/-CH$_2$ groups (1,482–1,450 cm^{-1}), aromatic > C=C< groups (1,540–1,487 cm^{-1}), aromatic rings (1,629–1,543 cm^{-1}), conjugated > C=O in ketone structures or carboxylic groups (1,713–1,644 cm^{-1}), unsaturated/saturated ester structures (1,766–1,727 cm^{-1}) and aryl ester structures (1,797–1,776 cm^{-1}) (Fig. 2 and Table S2). The RAs of unsaturated structures in SCR and BCs showed significant changes during the pyrolysis process (Table S2). The lower RA of deformed vibration asymmetric -CH$_3$ or -CH$_2$ groups (10.01%) was shown for BC700 compared to those found for BC500 (20.25%) (Table S2), which could attribute to the decomposition of small substituent groups on aromatic rings after the hotter pyrolysis (>400 °C) (Tian et al., 2016; Xiong et al., 2015). The aliphatic -CH$_3$ or -CH$_2$ groups were likely broken with IPT during the formation of larger aromatic ring systems. The pyrogenic amorphous carbon was turned into turbostratic crystallites in BCs at higher PTs (Xiao et al., 2014). This process likely involved volatilization of O in various compounds during pyrolysis, and a combination of reactive aromatic C with another active C for poly-condensation of aromatic structures (Zhao et al., 2016). For BCs, the RAs of aromatic > C=C< groups decreased from 50.21% to 0.4%, while the RAs of aromatic rings increased from 13.63% to 27.96% with IPT (Table S2), which were related to the formation of condensed aromatic rings at higher PTs (Tian et al., 2016). Conjugated > C=O may be present in aromatic ketone structures with >C=O on the α-carbon, alkenones with conjugated > C=C< groups, or carboxylic groups with conjugated > C=O (Liu et al., 2014). For example, the RAs of conjugated > C=O in ketones in BCs increased from 7.99% to 25.27% with IPT (Table S2). Both unsaturated and saturated ester structures were present in BCs, while aryl ester groups (42.34%) were the dominant structures in SCR (Table S2). Significant decomposition of aryl esters, and the general decrease of aromatic > C=C< groups with IPT, was related to the connection of adjacent aromatic groups by bridges at high PTs (Cao et al., 2012; Liu et al., 2014). While the heterogeneity of different BCs leads to difficulties in identifying the consistent changes for functional groups with pyrolysis temperatures, this study provides an effective method to distinguish and quantify the temperature-dependent changes of functional groups. Specifically, the advantages of using GM are revealing and quantifying the

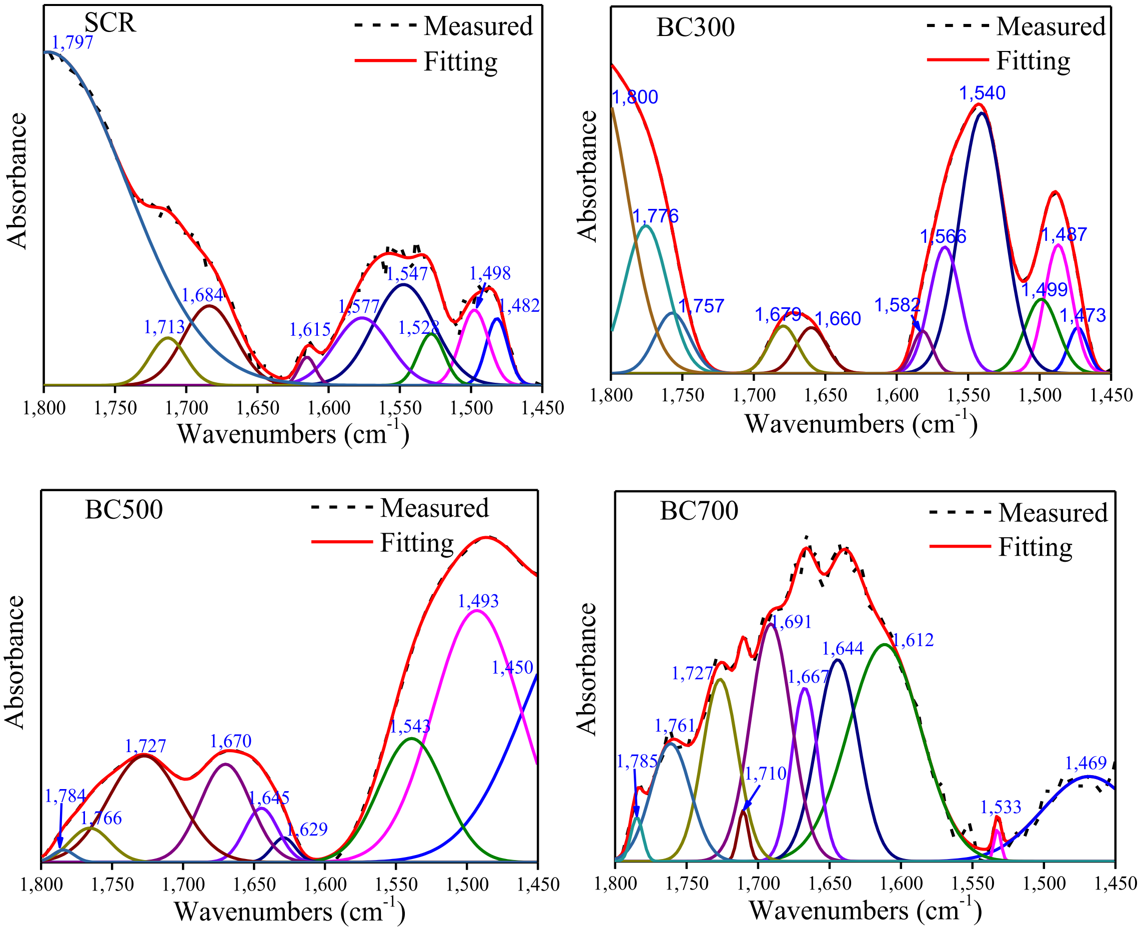

Fig. 2. Curve fitting of FTIR spectra of the SCR and BCs in the 1,800–1,450 cm^{-1} region.

overlapping and "hidden" peaks in spectra, thus allowing for a more thorough investigation of the varieties of various and specific functional groups during the formation of BCs through pyrolysis.

3.3. Evolution of carbon distributions and skeleton structure types in SCR and BCs

Patterns of solid-state ^{13}C NMR spectra of SCR and BC300 were similar to each other, but significantly different from those of BC500 and BC700 (Fig. 3). The ^{13}C NMR spectra of SCR and BCs were further divided into 9–13 individual Gaussian fitting peaks with coefficient of determination (R^2) ranging from 0.9729 to 0.9941 (Fig. 3 and Table 3). Individual fitted peaks associated with various carbon types were distinguished for aliphatic C (0–90 ppm), aromatic C (90–167 ppm), and carbonyl C (167–220 ppm) (Fig. 3). The sharpest fitting peak was observed at about 75 ppm, which was assigned to -CH_2OCH_2- (f_{ali}^{o2}) in SCR and BC300, while the strongest fitting peak related to aromatic bridgehead carbon (f_{ary}^{b}) was obtained at about 128 ppm in BC500 and BC700 (Fig. 3) (Liu et al., 2014).

In the aliphatic C region in SCR and BCs, the Gaussian fitting peaks for methylene C (f_{ali}^{1-3}, 47.7–12.8 ppm; f_{ali}^{1}: RCH_3, f_{ali}^{2}: -CH_2-, f_{ali}^{3}: tertiary CH and quaternary C), methyl C on aromatic rings (f_{ali}^{a}: 21.8 ppm, aromatic CH_3), and aliphatic C bound to oxygen (f_{ali}^{o}, 83.8–55.4 ppm; f_{ali}^{o1}: oxy-methylene, f_{ali}^{o2}: -CH_2OCH_2-, f_{ali}^{o3}: RCH_2OH or > CHOH) were observed (Fig. 3 and Table 3) (Liu et al., 2014; Tian et al., 2017). Table 3 reports the relative contents of the various types of carbon observed in the SCR and BCs. Specifically, the methyl C on aromatic rings (f_{ali}^{a}) with RAs of 1.90% was only observed for SCR, but these disappeared during pyrolysis of the BCs (Table 3). The amount of methylene C (f_{ali}^{1-3}) in SCR accounted for 1.51%, which was less than the same fraction within BCs (3.75%–19.85%) (Table 3). Moreover, the amounts of aliphatic C bound to oxygen (f_{ali}^{o}) in SCR and BC300 with RAs ranging from 30.03% to 65.34% were greater than those in either BC500 or BC700 (4.68%–9.59%) (Table 3). Tertiary and quaternary Cs appeared, while R-CH_2OH/>CHOH groups disappeared at the higher PTs for BC500 and BC700 (Table 3). These results demonstrated the depletion of methyl groups on aromatic rings, aliphatic groups bound to oxygen and R-CH_2OH/>CHOH structures during the formation of methylene groups, and tertiary/quaternary C structures all connected with IPT. In the aromatic C region, the protonated aromatic C (f_{ary}^{H1-H3}, 122.8–104.8 ppm), bridgehead aromatic C (f_{ary}^{b}, 134.9–126.6 ppm), alkylated aromatic C (f_{ary}^{a}, 150.5–140.4 ppm), and oxygen-substituted aromatic C (aromatic OH/OR) (f_{ary}^{o}, 155.0–151.7 ppm) were distinguished for SCR and BCs with the GM (Fig. 3 and Table 3) (Liu et al., 2014; Tian et al., 2016). RAs of carbon types in SCR, BC300, BC500, and BC700 exhibited the orders of $f_{ary}^{H} > f_{ary}^{b} \approx f_{ary}^{a}$, $f_{ary}^{H} > f_{ary}^{b} > f_{ary}^{a}$, $f_{ary}^{b} > f_{ary}^{H} > f_{ary}^{a}$, and $f_{ary}^{b} > f_{ary}^{a} > f_{ary}^{H}$, respectively (Table 3), which indicated that the protonated aromatic C was gradually decomposed as a function of IPT. The RAs of aromatic bridgehead C of SCR and BCs increased from 5.30% to 58.56% with IPT (Table 3). These results suggested that bridgehead aromatic C and oxygen-substituted aromatic C became more prevalent at higher temperatures, which was consistent with the results from the XPS and FTIR. The carbonyl C in carboxyls/esters

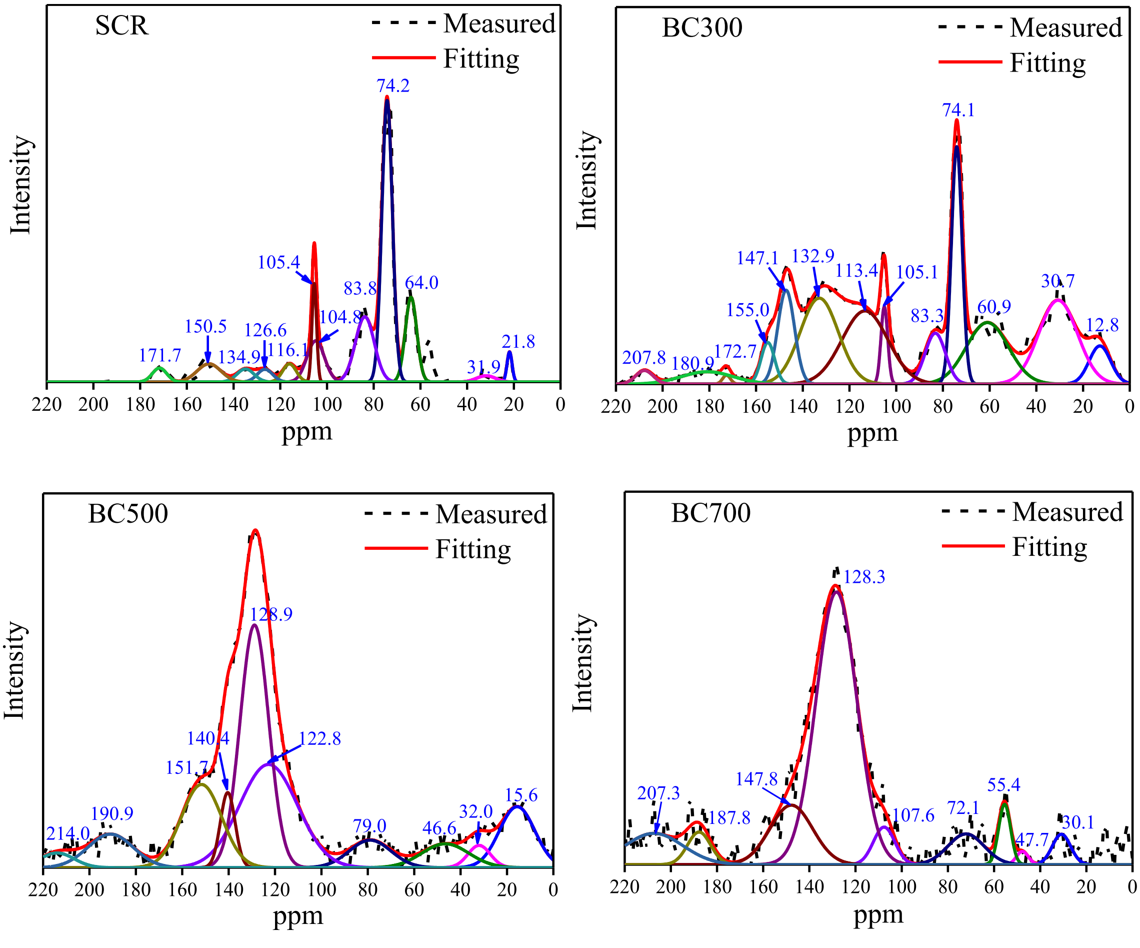

Fig. 3. Curve fitting of ^{13}C NMR spectra of SCR and BCs.

Table 3
Assignments and relative area of Gaussian fitting peaks from ^{13}C NMR spectra of SCR and BCs.

SCR				BC300				BC500				BC700			
CS (ppm)[a]	Assignment	Symbol	RA (%)[b]	CS (ppm)	Assignment	Symbol	RA (%)	CS (ppm)	Assignment	Symbol	RA (%)	CS (ppm)	Assignment	Symbol	RA (%)
21.8	aromatic CH_3	f_{ali}^{a}	1.90	12.8	RCH_3	f_{ali}^{1}	4.02	15.6	RCH_3	f_{ali}^{1}	8.84	30.1	$-CH_2-$	f_{ali}^{2}	2.93
31.9	$-CH_2-$	f_{ali}^{2}	1.51	30.7	$-CH_2-$	f_{ali}^{2}	15.83	32.0	$-CH_2-$	f_{ali}^{2}	2.03	47.7	tertiary CH and quaternary C	f_{ali}^{3}	0.82
64.0	CH_3OCH_2-	f_{ali}^{o1}	12.30	60.9	CH_3OCH_2-	f_{ali}^{o1}	12.66	46.6	tertiary CH and quaternary C	f_{ali}^{3}	4.58	55.4	CH_3OCH_2-	f_{ali}^{o1}	3.77
74.2	$-CH_2OCH_2-$	f_{ali}^{o2}	37.41	74.1	$-CH_2OCH_2-$	f_{ali}^{o2}	12.29	79.0	RCH_2OH or > CHOH	f_{ali}^{o3}	4.68	72.1	$-CH_2OCH_2-$	f_{ali}^{o2}	5.82
83.8	RCH_2OH or > CHOH	f_{ali}^{o3}	15.63	83.3	RCH_2OH or > CHOH	f_{ali}^{o3}	5.08	122.8	protonated aromatic	f_{ary}^{H3}	24.43	107.6	protonated aromatic	f_{ary}^{H2}	4.24
104.8	protonated aromatic	f_{ary}^{H1}	9.08	105.1	protonated aromatic	f_{ary}^{H2}	2.54	128.9	aromatic bridgehead	f_{ary}^{b}	28.48	128.3	aromatic bridgehead	f_{ary}^{b}	58.56
105.4	protonated aromatic	f_{ary}^{H2}	5.73	113.4	protonated aromatic	f_{ary}^{H3}	16.46	140.4	alkylated aromatic	f_{ary}^{a}	4.53	147.8	alkylated aromatic	f_{ary}^{a}	13.33
116.1	protonated aromatic	f_{ary}^{H3}	3.11	132.9	aromatic bridgehead	f_{ary}^{b}	16.06	151.7	aromatic OH or aromatic OR	f_{ary}^{o}	13.75	187.8	carbonyl in ester	f_{car}^{c1}	3.95
126.6	aromatic bridgehead	f_{ary}^{b}	2.49	147.1	alkylated aromatic	f_{ary}^{a}	7.69	190.9	carbonyl in ester	f_{car}^{c1}	6.22	207.3	carbonyl in ketone and aldehyde	f_{car}^{c2}	6.59
134.9	aromatic bridgehead	f_{ary}^{b}	2.81	155.0	aromatic OH or aromatic OR	f_{ary}^{o}	2.76	214.0	carbonyl in ketone and aldehyde	f_{car}^{c2}	2.47				
150.5	alkylated aromatic	f_{ary}^{a}	5.49	172.7	carbonyl in ester	f_{car}^{c1}	0.34								
171.7	carbonyl in ester	f_{car}^{c1}	2.55	180.9	carbonyl in ester	f_{car}^{c1}	3.12								
				207.8	carbonyl in ketone and aldehyde	f_{car}^{c2}	1.15								

[a] CS was chemical shift.

[b] Relative contents (RA) (%) of each peak was calculated as dividing peak area of each fitting peak by the sum of the peak area of all the fitting peaks.

(f_{car}^{c1}, 190.9–171.7 ppm) and in ketones/aldehydes (f_{car}^{c2}, 207.3–214.0 ppm) were also distinguished for SCR and BCs (Fig. 3 and Table 3) (Liu et al., 2014; Tian et al., 2016). The carbonyl C in esters, ketones, and aldehydes (f_{car}^{c1}) were dominant in BC500 with RA of 6.22% (Table 3). The RAs of carbonyl C in ketones/aldehydes (f_{car}^{c2}) in BCs increased from 1.15% to 6.59% with IPT (Table 3), indicating possible formation of ketone-like and/or aldehyde-like structures during pyrolysis of BCs.

To evaluate the carbon skeleton structures in SCR and BCs based on the Gaussian fitting results, several significant parameters of aromaticity (f_{ary}), aliphaticity (f_{ali}), the carbonylation ratio (f_{car}), aromatic edge carbons (χ_{edge}), the bridgehead aromatic carbon ratio (χ_b), the mean number of carbon atoms of methylene (C_n), and the substituted degree of aromatic rings (σ) were selected and presented in Table 4. Values of f_{ary} in SCR and BCs increased gradually from 28.71% to 76.13%; f_{car} values increased from 2.55% to 10.54%; and f_{ali} values decreased gradually from 68.75% to 13.14% with IPT (Table 4). As discussed below, these results were likely attributed to the increase of bridgehead aromatic carbons, the decrease of substituted edge aromatic carbons, and the broadening of the aromatic band, part of which was integrated as "oxygen-containing" functional groups (Cao et al., 2012). The number of aromatic edge carbons ($\chi_{edge} = 1\text{-}\chi_{bridge}$) was widely used to estimate the fraction of carbons along the edges of aromatic rings, which was inversely proportional to the size of aromatic ring clusters (Brewer et al., 2010; Cao et al., 2012). The χ_{edge} could be calculated from percentages of aromatic C-H, O-alkyl, alkyl, COO/NC=O, and C=O obtained from ^{13}C NMR spectra (Table S3) (Brewer et al., 2010; Qu et al., 2016). Therefore, the minimum and maximum χ_{edge} could be estimated by $\chi_{edge,min} = \chi_{CH} + \chi_{O\text{-}alkyl}$ and $\chi_{edge,max} = \chi_{edge,min} + \chi_{alkyl} + \chi_{COO/NC=O} + \chi_{C=O}$, respectively, in which χ represented the corresponding fraction of the given moiety normalized by the sum of aryl and O-aryl carbons of SCR and BCs (Brewer et al., 2010; Cao et al., 2012). $\chi_{edge,min}$ of SCR and BCs decreased from 0.64 to 0.16 with IPT (Table 4), indicating an increase in the fraction of bridgehead carbon and the aromatic ring cluster size (Cao et al., 2012). Cao et al. (2012) reported an increase of χ_{edge} at higher charring temperatures for wood chars produced at 300 °C and 700 °C. The minimum average aromatic cluster size ($n_{C,min}$), which was the stringent lower limit of cluster size within

Table 4
Important carbon structural parameters of SCR and BCs from analysis by Gaussian fitting peaks from ^{13}C NMR spectra.

Structural parameter	Definition	Value			
		SCR	BC300	BC500	BC700
aromaticity	$f_{ary} = f_{ary}^{H1} + f_{ary}^{H2} + f_{ary}^{H3} + f_{ary}^{b} + f_{ary}^{a} + f_{ary}^{o}$	28.71%	45.51%	71.19%	76.13%
aliphaticity	$f_{ali} = f_{ali}^{1} + f_{ali}^{a} + f_{ali}^{2} + f_{ali}^{3} + f_{ali}^{o1} + f_{ali}^{o2} + f_{ali}^{o3}$	68.75%	49.88%	20.13%	13.14%
carbonylation ratio	$f_{car} = f_{car}^{c1} + f_{car}^{c2}$	2.55%	4.61%	8.69%	10.54%
minimum aromatic edge carbons	$\chi_{edge,min} = \chi_{CH} + \chi_{O\text{-}alkyl}$	0.64	0.32	0.20	0.16
maximum aromatic edge carbons	$\chi_{edge,max} = \chi_{edge,min} + \chi_{alkyl} + \chi_{COO/NC=O} + \chi_{C=O}$	N.C.	N.C.	0.65	0.59
minimum average aromatic cluster size ($n_{C,min}$)	$3/(\chi_{edge}\text{-}0.5) \geq n_{C,min} \geq 6/(\chi_{edge})^2 \geq 6/(\chi_{edge,max})^2$	N.C.	N.C.	>14	>17
bridgehead aromatic carbon ratio	$\chi_b = f_{ary}^{b}/f_{ary}$	0.18	0.35	0.40	0.77
average carbon number of methylene	$C_n = f_{ali}^{2}/f_{ary}^{a}$	0.28	2.06	0.45	0.22
substituted degree of aromatic rings	$\sigma = (f_{ary}^{a} + f_{ary}^{o})/f_{ary}$	0.19	0.23	0.26	0.18

N.C. represented non-calculable.

the SCR and BCs, could be estimated by $3/(\chi_{edge}\text{-}0.5) \geq n_{C,min} \geq 6/(\chi_{edge})^2 \geq 6/(\chi_{edge,max})^2$ (Brewer et al., 2010). BC500 and BC700 had an average of more than 14 carbons in an average aromatic cluster, indicating more than three aromatic rings might be expected (Table 4). $n_{C,min}$ values of SCR and BC300 could not be estimated, a result that was in agreement with the lower aromaticity observed in SCR and BC300 (Table 4). It suggested that the relatively high degree of condensation for SCR was unclear, and BC300 might consist primarily of small average aromatic domains and aromatic rings substituted by carboxylic groups, and by phenolic groups to a lesser extent (Qu et al., 2016). Additionally, the bridgehead aromatic carbon ratio (χ_b) increased from 0.18 to 0.77 with IPT (Table 4), which was consistent with the decrease of $\chi_{edge,min}$ values. The mean number of methylene carbons of BC300 ($C_n = 2.06$) was greater than those found in BC500 or BC700 ($C_n = 0.22$–0.45) (Table 4), which could be attributed to the increase of aromatic rings in BCs, as well as the decrease in short-branched aliphatic C at higher PTs. The degree of substitution of aromatic rings (σ) of SCR and BCs ranged from 0.18 to 0.26 (Table 4), which were less than the σ value ($\sigma = 0.5$) of lignite reported in previous study (Li et al., 2018), suggesting fewer substituent groups on each aromatic ring in SCR and BCs with IPT, especially for BC700. It had reported that macromolecular aromatics were difficult to degrade even by thermal dissolution (Tian et al., 2016); therefore, greater amounts of macromolecular aromatics appeared in BCs as PTs increases. The carbon skeleton structures vary among various BC products due to the presence of heterogeneity, but a number of important experimental data regarding the structural and chemical characterization in this study will facilitate the comparative study of carbon skeletons among different BCs and better understand the further effects of BCs on the migration, transformation and bioavailability of pollutants in soil environment.

3.4. Determination of pyrolysis behaviors and kinetics of SCR and BCs

Obvious differences in the TG, DTG curves, and Coats-Redfern plots were observed for thermal degradation of SCR and BCs (Fig. 4). The final mass residues following the pyrolysis at 850 °C of SCR, BC300, BC500, and BC700 were about 22.30%, 67.52%, 79.60% and 87.69% to total mass, respectively, showing the order of thermal stability as BC700 > BC500 > BC300 > SCR (Fig. 4a). The thermal stability of SCR and BCs was confirmed by their degree of aromatic condensation from the ^{13}C NMR analysis as discussed above. Therefore, the BCs produced at higher temperatures consisted of a more stable form of carbon with higher resistance to heat. Furthermore, for BCs, the mass decomposition to total mass of BC700 before 400 °C (9.13%) was slightly larger than those of BC300 and BC500 (6.01%–8.55%), which was likely due to the different degree of moisture evaporation from ambient temperature to 120 °C as results from the DTG curves of BCs (Fig. 4a) (Gao et al., 2013). Additionally, the pyrolysis process estimated from the DTG curves of SCR and BCs consisted of three stages: 140–315 °C, 315–370 °C and 370–850 °C (Fig. 4a). In contrast to the sharper DTG peaks of SCR in the first and second stages (fast de-volatilization stages), weaker DTG peaks of BCs at in the third stage (slow degradation stage) were observed (Fig. 4a). The mass decompositions to total mass of SCR during the first (30.47%) and second (34.56%) stages were mainly attributed to degradation of hemicellulose and cellulose, respectively (Fig. 4a) (Gao et al., 2013). Thermal degradation of cellulose was more difficult than that of hemicellulose in SCR, due to a higher degree of polymerization and crystalline structures with ordered micro-fibrils in the cellulose (Ma et al., 2015). The weight losses of BCs during the first and second stages were less than 5% (Fig. 4a). Weight loss of SCR, BC300, BC500, and BC700 in the third stage was 23.77%, 25.88%, 15.12%, and 3.43% to total mass, respectively (Fig. 4a), which was associated with the degradation of lignin (Ma et al., 2015). Furthermore, during the pyrolysis process, the fast de-volatilization stages were mainly associated with bond breakage, de-polymerization, and fragmentation of -OCH$_3$ and acetyl, whereas the slow degradation stage was focus on the condensation of polycyclic structure and conversion of short substituents of benzene rings. It could be concluded that the aliphatic and aromatic carbons in SCR and BCs were gradually converted into transited carbons, then into increasingly condensed forms of carbon during the pyrolysis process. The E_a and pre-exponential factor (A) of SCR and BCs were calculated at different temperature ranges ($R^2 = 0.949$–0.998) (Fig. 4b and Table S4). Values of A for SCR and BCs pyrolysis were 0.81–2.47×10^4 min^{-1}, indicating the surface reactions for pyrolysis process (Table S4). Similarly, values of E_a for SCR and BCs pyrolysis varied from 23.01 kJ mol^{-1} to 60.53 kJ mol^{-1} (Table S4), showing significant decreases from SCR to BC500, and slight increase at 750°C–850 °C for BC700. The higher E_a value for SCR decomposition is mainly due to the higher thermal stability of chemical structures of cellulose. The decreases of E_a values for BCs as the temperature increased are mainly due to the already start of cellulose decomposition for BC300, and the almost completed

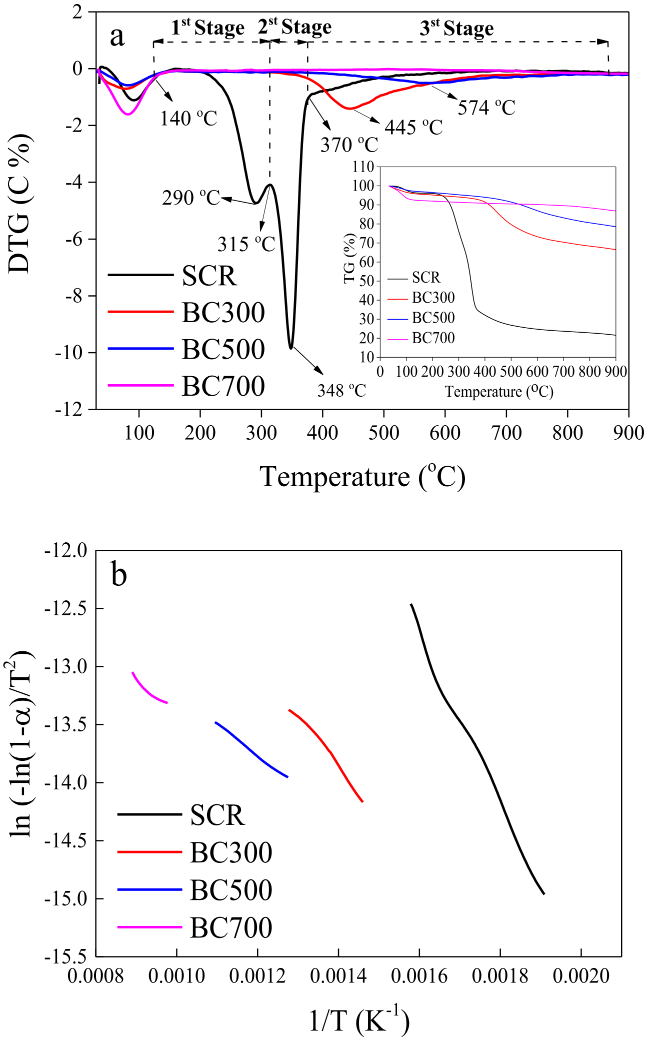

Fig. 4. TG, DTG curves (a) and Coats-Redfern plots (b) for thermal degradation of SCR and BCs at different ranges of pyrolysis temperatures.

decomposition of cellulose for BC500 and BC700. The differences for the E_a values during the conversion of SCR into BCs are likely associated to the incomplete pyrolysis of SCR and the additional heterogeneity of BCs that likely impedes a good characterization of BCs. Therefore, BC pyrolysis was a complicated physicochemical process that was associated to the pyrolysis mechanisms of the main biomass components (i.e., cellulose, hemicellulose, and lignin). The information on thermal decomposition gained from this study was very helpful and significant to designing a successful future manufacturing process for bioenergy and products made from SCR and BCs.

4. Conclusions

The structural, functional characteristics and pyrolysis kinetics of dried sugarcane residue (SCR) and SCR-derived BCs (BC300, BC500, and BC700) were investigated. The novelty of this study is that the novel XPS/FTIR/NMR—Gaussian method was applied to deconvolute the existences and contributions of distinct peaks in spectra, and then quantify the content of specific functional groups and skeleton structures of SCR and BCs. Aromatic C/C=C (64.94—93.68%), single bonded O (48.45—86.56%) and pyrrolic N (>61.31%) were dominant for elemental C, O and N on SCR and BCs surfaces, respectively. Decomposition (e.g., free -OH/-OH … π groups) and formation (e.g., conjugated > C=O in ketones) of functional groups were quantitatively distinguished for BCs with higher pyrolysis temperatures. Progressive dehydration, decarboxylation, aromatization reactions and structural formations of condensed carbon resulted in the changes of carbon structures and types of SCR and BCs. More fractions of bridgehead carbon, aromatic ring cluster size and macromolecular aromatics were presented in BCs produced at higher pyrolysis temperatures. Fewer substituent groups at each aromatic ring were for SCR and BCs, and the BC500 and BC700 had an average of more than 14 carbons in average aromatic cluster. The activation energy for pyrolysis reactions of SCR and BCs varied from 23.01 kJ mol^{-1} to 60.53 kJ mol^{-1}, which were attributed to the degradation of hemicellulose, cellulose and lignin components in SCR and BCs. Elucidating the distinct composition, structural and functional properties of biomass and BCs will help more accurately optimize the production and pyrolysis process, and evaluate the potential performances of BCs in many scientific research and engineering applications. In addition, the application of XPS/FTIR/NMR—Gaussian method presented in this study has shown potential to be used as a valuable and effective characterization technique for studying the possible carbon sequestration or interactions between pollutants and BCs when the BCs are utilized as additive or adsorbent in soil or aquatic systems. It should be pointed out that the heterogeneous properties of BCs are associated to the individual BCs particles and the originating feedstocks or different pyrolysis conditions, resulting in somewhat unpredictable risks once deployed BCs into environments. Therefore, in the future, a comprehensive investigation of the characteristics and pyrolysis kinetics of BCs produced from more different biomasses or pyrolysis conditions is necessary to be conducted for supporting their efficient applications.

Acknowledgements

This work was financially supported by the National Natural Science Foundation of China (Nos. 41521003, 41630645 and 41573130). Thanks for Dr. Weiying Feng, Dr. Shasha Liu, Dr. Ning Qin and Dr. Jia He from Chinese Research Academy of Environmental Sciences for their analysis of Fourier transform infrared spectroscopy and X-ray photon spectroscopy. Additionally, sincere thanks to the editor Prof. Sharifah Rafidah Wan Alwi and the anonymous reviewers for their useful comments and suggestions to improve the paper.

Appendix A. Supplementary data

Supplementary data to this article can be found online at https://doi.org/10.1016/j.jclepro.2019.117855.

References

Ahmad, M., Rajapaksha, A.U., Lim, J.E., Zhang, M., Bolan, N., Mohan, D., Vithanage, M., Lee, S.S., Ok, Y.S., 2014. Biochar as a sorbent for contaminant management in soil and water: a review. Chemosphere 99, 19—33.

Alam, M.S., Gorman-Lewis, D., Chen, N., Flynn, S.L., Ok, Y.S., Konhauser, K.O., Alessi, D.S., 2018. Thermodynamic analysis of Nickel(II) and Zinc(II) adsorption to biochar. Environ. Sci. Technol. 52, 6246—6255.

Bachmann, H.J., Bucheli, T.D., Dieguez-Alonso, A., Fabbri, D., Knicker, H., Schmidt, H.P., Ulbricht, A., Becker, R., Buscaroli, A., Buerge, D., Cross, A., Dickinson, D., Enders, A., Esteves, V.I., Evangelou, M.W.H., Fellet, G., Friedrich, K., Gasco Guerrero, G., Glaser, B., Hanke, U.M., Hanley, K., Hilber, I., Kalderis, D., Leifeld, J., Masek, O., Mumme, J., Carmona, M.P., Calvelo Pereira, R., Rees, F., Rombolà, A.G., de la Rosa, J.M., Sakrabani, R., Sohi, S., Soja, G., Valagussa, M., Verheijen, F., Zehetner, F., 2016. Toward the standardization of biochar analysis: the COST action TD1107 interlaboratory comparison. J. Agr. Food Chem. 64 (2), 513—527.

Balsari, P., Airoldi, G., Dinuccio, E., Gioelli, F., 2007. Ammonia emissions from farmyard manure heaps and slurry stores—effect of environmental conditions and measuring methods. Biosyst. Eng. 97 (4), 456—463.

Brewer, C.E., Schmidt-Rohr, K., Satrio, J.A., Brown, R.C., 2010. Characterization of biochar from fast pyrolysis and gasification systems. Environ. Prog. Sustain. Energy 28, 386—396.

Calvelo Pereira, R., Kaal, J., Camps Arbestain, M., Pardo Lorenzo, R., Aitkenhead, W., Hedley, M., Macías, F., Hindmarsh, J., Maciá-Agulló, J.A., 2011. Contribution to characterisation of biochar to estimate the labile fraction of carbon. Org. Geochem. 42 (11), 1331—1342.

Cao, X., Pignatello, J.J., Li, Y., Lattao, C., Chappell, M.A., Chen, N., Miller, L.F., Mao, J., 2012. Characterization of wood chars produced at different temperatures using advanced solid-state ^{13}C NMR spectroscopic techniques. Energy Fuel. 26, 5983—5991.

Chen, L., Xing, L., Han, L., 2009. Renewable energy from agro-residues in China: solid biofuels and biomass briquetting technology. Renew. Sustain. Energy Rev. 13 (9), 2689—2695, 2009.

Chen, Z., Xiao, X., Chen, B., Zhu, L., 2015. Quantification of chemical states, dissociation constants and contents of oxygen-containing groups on the surface of biochars produced at different temperatures. Environ. Sci. Technol. 49, 309—317.

Coats, A.W., Redfern, J.P., 1964. Kinetic parameters from thermogravimetric data. Nature 201, 68—69.

Galil, N., Yaacov, L., 2011. Analysis of sludge management parameters resulting from the use of domestic garbage disposers. Water Sci. Technol. 44 (10), 27—34.

Gao, N., Li, A., Quan, C., Du, L., Duan, Y., 2013. TG-FTIR and Py-GC/MS analysis on pyrolysis and combustion of pine sawdust. J. Anal. Appl. Pyrol. 100, 26—32.

Giudicianni, P., Bozza, P., Sorrentino, G., Ragucci, R., 2015. Thermal and mechanical stabilization process of the organic fraction of the municipal solid waste. Waste Manag. 44, 125—134.

Jin, J., Li, Y., Zhang, J., Wu, S., Cao, Y., Liang, P., Zhang, J., Wong, M.H., Wang, M., Shan, S., 2016. Influence of pyrolysis temperature on properties and environmental safety of heavy metals in biochars derived from municipal sewage sludge. J. Hazard Mater. 320, 417—426.

Jin, J., Sun, K., Yang, Y., Wang, Z., Han, L., Wang, X., Wu, F., Xing, B., 2018. Comparison between soil- and biochar-derived humic acids: composition, conformation, and phenanthrene sorption. Environ. Sci. Technol. 52, 1880—1888.

Joeri, K., Roberto, C., Art, D., Anna, M., Antonio Martínez, C., Hugh, M., 2017. Multimethodological characterisation of Costa Rican biochars from small-scale retort and top-lit updraft stoves and inter-methodological comparison. J. Agr. Rural Dev. Trop. Subtrop. 118 (1), 1—15.

Kloss, S., Zehetner, F., Dellantonio, A., Hamid, R., Ottner, F., Liedtke, V., Schwanninger, M., Gerzabek, M.H., Soja, G., 2012. Characterization of slow pyrolysis biochars: effects of feedstocks and pyrolysis temperature on biochar properties. J. Environ. Qual. 41, 990—1000.

Krishna, S., Pugazhenthi, G., 2011. Properties and thermal degradation kinetics of polystyrene/organoclay nanocomposites synthesized by solvent blending method: effect of processing conditions and organoclay loading. J. Appl. Polym. Sci. 120, 1322—1336.

Li, S., Zong, Z.M., Liu, J., Wei, X.Y., 2018. Characterization of nitrogen and sulfur-containing species in Zhaotong lignite and its extracts from ultrasonic extraction. Fuel 219, 417—425.

Liu, F.J., Wei, X.Y., Xie, R.L., Wang, Y.G., Li, W.T., Li, Z.K., Li, P., Zong, Z.M., 2014. Characterization of oxygen-containing species in methanolysis products of the extraction residue from Xianfeng lignite with negative-ion electrospray ionization fourier transform ion cyclotron resonance mass spectrometry. Energy Fuel. 28, 5596—5605.

Liu, S., Zhu, Y., Liu, L., He, Z., Giesy, J.P., Bai, Y., Sun, F., Wu, F., 2018. Cation-induced coagulation of aquatic plant-derived dissolved organic matter: investigation by EEM-PARAFAC and FT-IR spectroscopy. Environ. Pollut. 234, 726–734.

Liu, S., Zhu, Y., Meng, W., He, Z., Feng, W., Zhang, C., Giesy, J.P., 2016. Characteristics and degradation of carbon and phosphorus from aquatic macrophytes in lakes: insights from solid-state ^{13}C NMR and solution ^{31}P NMR spectroscopy. Sci. Total Environ. 543, 746–756.

Ma, Z., Chen, D., Gu, J., Bao, B., Zhang, Q., 2015. Determination of pyrolysis characteristics and kinetics of palm kernel shell using TGA-FTIR and model-free integral methods. Energy Convers. Manag. 89, 251–259.

Norwood, M.J., Louchouarn, P., Kuo, L.J., Harvey, O.R., 2013. Characterization and biodegradation of water-soluble biomarkers and organic carbon extracted from low temperature chars. Org. Geochem. 56, 111–119.

Qu, X., Fu, H., Mao, J., Ran, Y., Zhang, D., Zhu, D., 2016. Chemical and structural properties of dissolved black carbon released from biochars. Carbon 96, 759–767.

Sánchez-Jiménez, P.E., Pérez-Maqueda, L.A., Perejón, A., Criado, J.M., 2013. Limitations of model-fitting methods for kinetic analysis: polystyrene thermal degradation. Resour. Conserv. Recy. 74, 75–81.

Scotto Di Perta, E., Agizza, M.A., Sorrentino, G., Boccia, L., Pindozzi, S., 2016. Study of aerodynamic performances of different wind tunnel configurations and air inlet velocities, using computational fluid dynamics (CFD). Comput. Electron. Agr. 125, 137–148.

Şensöz, S., Angın, D., Yorgun, S., 2000. Influence of particle size on the pyrolysis of rapeseed (*Brassica napus L.*): fuel properties of bio-oil. Biomass Bioenergy 19, 271–279.

Shen, T., Tang, Y., Lu, X.Y., Meng, Z., 2018. Mechanisms of copper stabilization by mineral constituents in sewage sludge biochar. J. Clean. Prod. 193, 185–193.

Singh, B., Fang, Y., Cowie, B.C.C., Thomsen, L., 2014. NEXAFS and XPS characterisation of carbon functional groups of fresh and aged biochars. Org. Geochem. 77, 1–10.

Singh, B.P., Cowie, A.L., 2014. Long-term influence of biochar on native organic carbon mineralisation in a low-carbon clayey soil. Sci. Rep. 3687.

Song, F., Wu, F., Feng, W., Liu, S., He, J., Li, T., Zhang, J., Wu, A., Amarasiriwardena, D., Xing, B., Bai, Y., 2019. Depth-dependent variations of dissolved organic matter composition and humification in a plateau lake using fluorescence spectroscopy. Chemosphere 225, 507–516.

Tang, Y., Alam, M.S., Konhauser, K.O., Alessi, D.S., Xu, S., Tian, W., Liu, Y., 2019. Influence of pyrolysis temperature on production of digested sludge biochar and its application for ammonium removal from municipal wastewater. J. Clean. Prod. 209, 927–936.

Thakur, L.S., Varma, A.K., Mondal, P., 2018. Analysis of thermal behavior and pyrolytic characteristics of vetiver grass after phytoremediation through thermogravimetric analysis. J. Therm. Anal. Calorim. 131, 3053–3064.

Tian, B., Qiao, Y., Bai, L., Liu, F., Tian, Y., Xie, K., 2017. Separation and structural characterization of groups from a high-volatile bituminous coal based on multiple techniques. Fuel Process. Technol. 159, 386–395.

Tian, B., Qiao, Y.Y., Tian, Y.Y., Xie, K.C., Liu, Q., Zhou, H.F., 2016. FTIR study on structural changes of different-rank coals caused by single/multiple extraction with cyclohexanone and NMP/CS2 mixed solvent. Fuel Process. Technol. 154, 210–218.

Verheijen, F., Jeffery, S., Bastos, A., Van der Velde, M., Diafas, I., 2010. Biochar application to soils. A critical scientific review of effects on soil properties, processes, and functions. EUR 24099, 162.

Wang, X., Chen, G., Wang, S., Zhang, L., Zhang, R., 2019. Temperature sensitivity of different soil carbon pools under biochar addition. Environ. Sci. Pollut. Res. 26 (4), 4130–4140.

Waqas, M., Aburiazaiza, A.S., Miandad, R., Rehan, M., Barakat, M.A., Nizami, A.S., 2018. Development of biochar as fuel and catalyst in energy recovery technologies. J. Clean. Prod. 188, 477–488.

Wu, W., Yang, M., Feng, Q., Mcgrouther, K., Wang, H., Lu, H., Chen, Y., 2012. Chemical characterization of rice straw-derived biochar for soil amendment. Biomass Bioenerg. 47, 268–276.

Xiao, X., Chen, B.L., Zhu, L.Z., 2014. Transformation, morphology, and dissolution of silicon and carbon in rice straw-derived biochars under different pyrolytic temperatures. Environ. Sci. Technol. 48, 3411–3419.

Xiong, G., Li, Y., Jin, L., Hu, H., 2015. In situ FT-IR spectroscopic studies on thermal decomposition of the weak covalent bonds of brown coal. J. Anal. Appl. Pyrol. 115, 262–267.

Zhao, B., O'Connor, D., Zhang, J., Peng, T., Shen, Z., Tsang, D.C.W., Hou, D., 2018. Effect of pyrolysis temperature, heating rate, and residence time on rapeseed stem derived biochar. J. Clean. Prod. 174, 977–987.

Zhao, Y., Feng, D., Zhang, Y., Huang, Y., Sun, S., 2016. Effect of pyrolysis temperature on char structure and chemical speciation of alkali and alkaline earth metallic species in biochar. Fuel Process. Technol. 141, 54–60.

Supporting Information

Spectroscopic analyses combined with Gaussian and Coats-Redfern models to investigate the characteristics and pyrolysis kinetics of sugarcane residue-derived biochars

Fanhao Song[1,2], Xiaojie Wang[3], Tingting Li[1], Jin Zhang[1], Yingchen Bai[1*], Baoshan Xing[4], John P. Giesy[1,5], Fengchang Wu[1]

[1]State Key Laboratory of Environmental Criteria and Risk Assessment, Chinese Research Academy of Environmental Sciences, Beijing, 10012, China

[2]College of Water Sciences, Beijing Normal University, Beijing, 100875, China

[3]Guangdong Provincial Key Laboratory of Environmental Pollution Control and Remediation Technology, School of Environmental Science and Engineering, Sun Yat-Sen University, Guangzhou 510006, China

[4]Stockbridge School of Agriculture, University of Massachusetts, Amherst, MA, 01003, USA

[5]Department of Biomedical and Veterinary Biosciences and Toxicology Centre, University of Saskatchewan, Saskatoon, Saskatchewan, SK, S7N 5B3, Canada

Number of Pages (including this cover sheet): 8

Number of Figs.: 2; Number of Tables: 4

[*]Corresponding author: Tel.: +86-10-84931804; Fax: +86-10-84931804.

E-mail: baiyc@craes.org.cn (Yingchen Bai).

Figures

Fig. S1. Van Krevelen plot of elemental ratios for SCR and BCs.

Fig. S2. Curve fitting of FTIR spectra of SCR and BCs in the 3,730-2,400 cm^{-1} region.

Tables

Table S1. Assignments and relative areas of Gaussian fitting peaks from XPS C1s, O1s and N1s spectra of SCR and BCs.

Table S2. Assignments and relative areas of Gaussian fitting peaks at 1,800-1,450 cm^{-1} region in the FTIR spectra of SCR and BCs.

Table S3. Carbon distributions (in % of total C) in SCR and BCs calculated by solid-state ^{13}C NMR spectroscopy.

Table S4. Kinetic analysis of SCR and BCs pyrolysis and combustion.

Figures

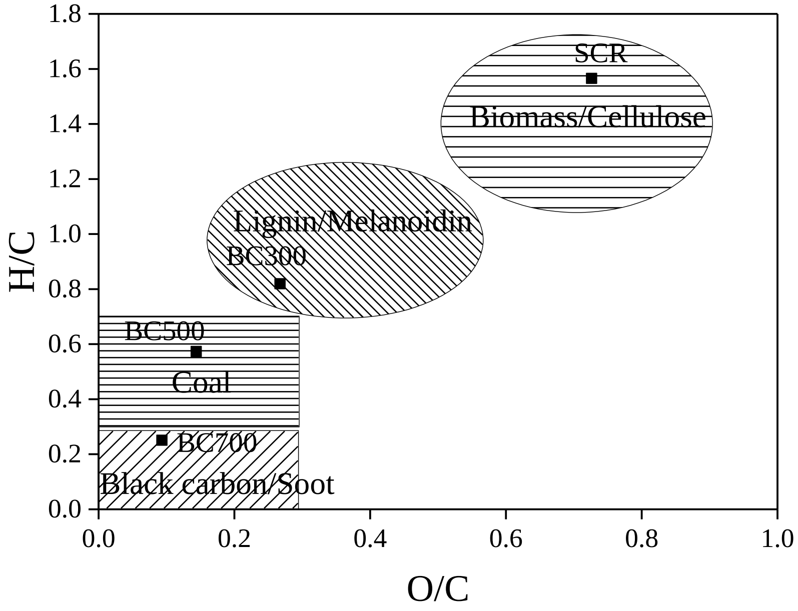

Fig. S1. Van Krevelen plot of elemental ratios for SCR and BCs.

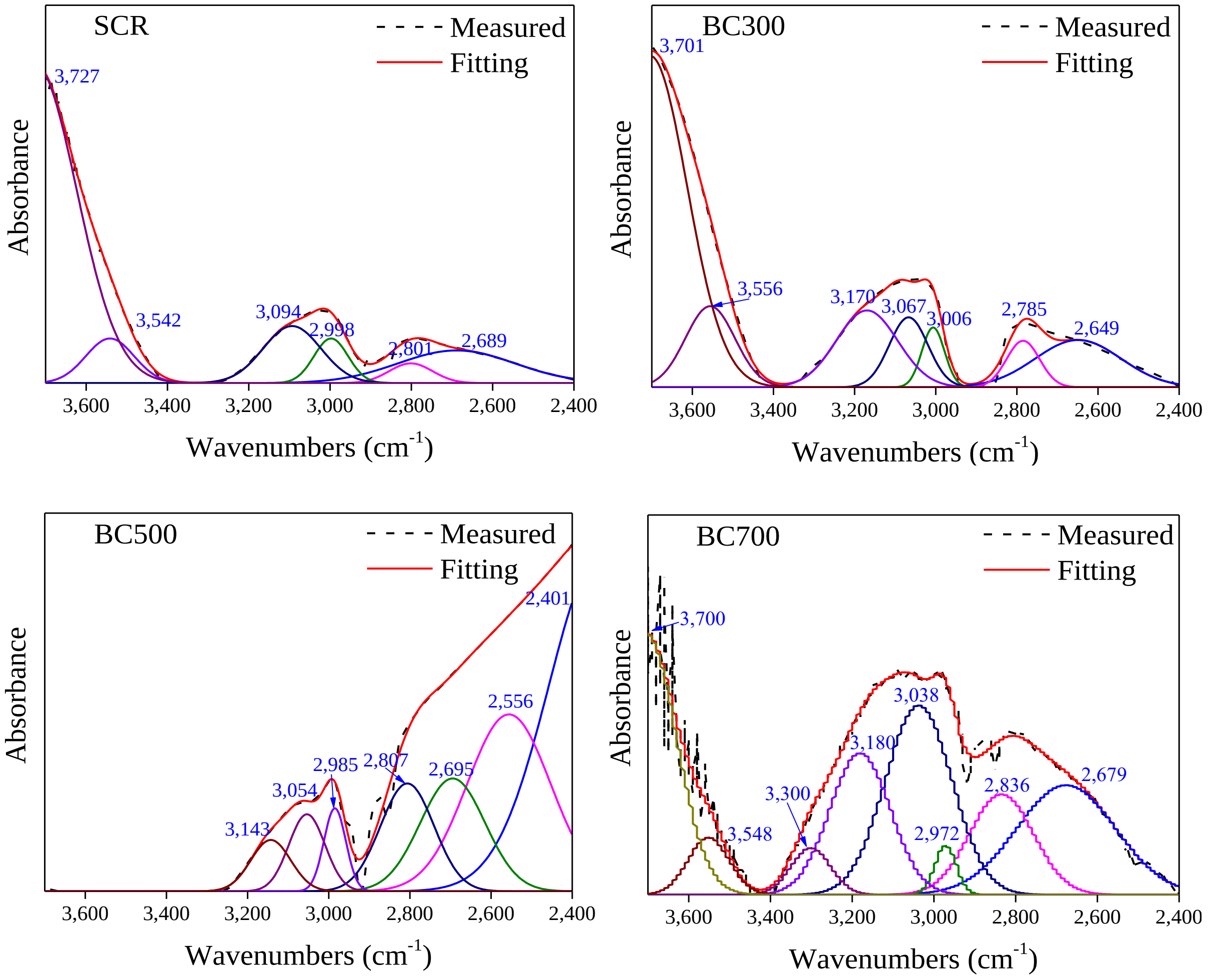

Fig. S2. Curve fitting of FTIR spectra of SCR and BCs in the 3,730-2,400 cm^{-1} region.

Tables

Table S1. Assignments and relative areas of Gaussian fitting peaks from XPS C1s, O1s and N1s spectra of SCR and BCs.

Elemental peaks	Sample	Binding energy (eV)	Functionalities	RA (%)[a]
C 1s	SCR	284.8	C=C, aromatic C	64.94
		286.4	phenolic C	30.50
		287.8	aliphatic and carboxylic C	4.55
	BC300	284.8	C=C, aromatic C	93.68
		286.4	phenolic C	6.32
	BC500	284.8	C=C, aromatic C	83.00
		286.0	phenolic C	17.00
	BC700	284.8	C=C, aromatic C	78.35
		285.9	phenolic C	2.87
		286.4	phenolic C	18.78
N 1s	SCR	400.1	pyrrolic N	100
	BC300	394.3	-N=N-	9.95
		400.1	pyrrolic N	90.05
	BC500	400.1	pyrrolic N	61.31
		406.0	chemisorbed N	38.69
	BC700	400.7	pyrrolic N	83.18
		403.5	chemisorbed N	2.19
		406.5	chemisorbed N	14.63
O 1s	SCR	531.3	carbonyl (>C=O) O	13.44
		532.8	hydroxyl (C-OH) O	86.56
	BC300	531.3	carbonyl (>C=O) O	24.33
		533.1	ether (C-O-)	75.67
	BC500	531.3	carbonyl (>C=O) O	25.59
		531.9	carbonyl (>C=O) O	16.36
		533.1	ether (C-O-)	48.45
		533.9	carboxyl (COOH) O	9.60
	BC700	531.3	carbonyl (>C=O) O	36.89
		533.1	ether (C-O-)	63.11

[a] Relative contents (RA) (%) of each peak was calculated as the ratio of each peak area at corresponding energy position to the total area of C1s, N1s and O1s peaks.

Table S2. Assignments and relative areas of Gaussian fitting peaks at 1,800-1,450 cm^{-1} region in the FTIR spectra of SCR and BCs.

SCR			BC300			BC500			BC700		
Wav. (cm^{-1})[a]	Assignment	RA (%)[b]	Wav. (cm^{-1})[a]	Assignment	RA (%)[b]	Wav. (cm^{-1})[a]	Assignment	RA (%)[b]	Wav. (cm^{-1})[a]	Assignment	RA (%)[b]
1,482	deformation vibration asymmetric- CH_3 or -CH_2	3.95	1,473	deformation vibration asymmetric- CH_3 or -CH_2	2.52	1,450	deformation vibration asymmetric -CH_3 or -CH_2	20.25	1,469	deformation vibration asymmetric-CH_3 or -CH_2	10.01
1,498	aromatic >C=C<	5.82	1,487	aromatic >C=C<	10.14	1,493	aromatic >C=C<	37.75	1,533	aromatic >C=C<	0.40
1,528	aromatic >C=C<	3.72	1,499	aromatic >C=C<	7.06	1,543	aromatic rings	13.74	1,612	aromatic rings	27.96
1,547	aromatic rings	16.68	1,540	aromatic >C=C<	33.01	1,629	aromatic rings	0.98	1,644	highly conjugated >C=O	14.86
1,577	aromatic rings	10.19	1,566	aromatic rings	11.21	1,645	highly conjugated >C=O	3.08	1,667	highly conjugated >C=O in aromatic ketones	8.10
1,615	aromatic rings	1.29	1,582	aromatic rings	2.42	1,670	highly conjugated >C=O in aromatic ketones	8.49	1,691	conjugated >C=O in aromatic ketones	17.17
1,684	conjugated >C=O in aromatic ketones	11.34	1,660	highly conjugated >C=O in aromatic ketones	4.04	1,727	unsaturated esters	12.90	1,710	>C=O in carboxylic acids	0.94
1,713	>C=O in carboxylic acids	4.67	1,679	highly conjugated >C=O in aromatic ketones	3.95	1,766	saturated esters	2.35	1,727	unsaturated esters	11.37
1,797	aryl esters	42.34	1,757	saturated esters	6.01	1,784	aryl esters	0.46	1,761	saturated esters	8.25
			1,776	aryl esters	18.19				1,785	aryl esters	0.93
			1,800	C=O	1.44						

[a] Wav. was wavenumbers.

[b] Relative area (RA) (%) of each peak was calculated as dividing peak area of each fitting peak by the sum of the peak area of all the fitting peaks.

Table S3. Carbon distributions (in % of total C) in SCR and BCs calculated by solid-state ^{13}C NMR spectroscopy.

Sample	Moieties location (ppm) (%)						
	0-45	45-90	90-110	110-148	148-167	167-184	184-220
	Alkyl C	O-alkyl C	Aryl CH	Aryl C	O-aryl C	COO/NC=O	C=O
SCR	1.39	67.07	14.58	10.10	3.65	1.90	1.32
BC300	22.27	31.40	8.69	30.29	5.79	0.67	0.89
BC500	13.25	7.68	4.64	55.23	9.14	2.65	7.42
BC700	7.69	11.11	4.35	58.66	6.96	1.32	10.10

Table S4. Kinetic analysis of SCR and BCs pyrolysis and combustion.

Sample (Temperature)	SCR (250-360^{o}C)	BC300 (410-550^{o}C)	BC500 (510-640^{o}C)	BC700 (750-850^{o}C)
Slope	-7,280	-4,525	-2,768	-2,931
Intercept	-1.08	-7.53	-10.45	-10.48
R^2	0.993	0.987	0.998	0.949
Ea (KJ·mol^{-1})	60.53	37.62	23.01	24.37
A (min^{-1})	24,705.24	24.29	0.81	0.82